ACCSCIENCE PUBLISHING

Materials Science in Additive Manufacturing

ORIGINAL RESEARCH ARTICLE

Anisotropy of room- and high-temperature mechanical properties in GH5188 superalloy fabricated by laser powder bed fusion

Gao Huang[1,2], Huihui Yang[3], Xiaojie Nie[4], and Yang Qi[5]*

[1]Wuhan National Laboratory for Optoelectronics, School of Optical and Electronic Information, Huazhong University of Science and Technology, Wuhan, Hubei, China

[2]Huagong Technology Industry Co., Ltd., Wuhan, Hubei, China

[3]Suzhou National Laboratory, Suzhou, Jiangsu, China

[4]Naval University of Engineering, Wuhan, Hubei, China

[5]Taihang Laboratory, Chengdu, Sichuan, China

Abstract

Laser powder bed fusion (LPBF) enables near-net-shape fabrication of GH5188 for hot-section applications, but orientation-dependent mechanical reliability remains insufficiently quantified. In this study, tensile tests were conducted at room temperature and 900 °C along the horizontal and vertical directions for LPBF-fabricated GH5188 in the as-fabricated (AF) and heat-treated (HT) states, and the results were correlated with microstructural characterization by scanning electron microscopy and electron backscatter diffraction. The results showed that the AF condition exhibited high strength with weak tensile anisotropy at room temperature and 900 °C. Heat treatment markedly reduced YS and improved ductility at both temperatures, and it also led to a more evident orientation dependence at 900 °C. Microstructural analyses indicated that the AF state presented LPBF hierarchical features that contribute to high initial flow resistance, whereas heat treatment removed these features and produced section-dependent grain and grain-boundary evolution, increasing the relative influence of grain-scale deformation at high temperature. This study provides an orientation-dependent AF/HT dataset and a microstructure-based interpretation of anisotropy evolution in LPBF GH5188, which is relevant to the qualification and design of high-temperature additive manufacturing components.

Keywords: GH5188; Laser powder bed fusion; Anisotropy; Mechanical properties; Microstructure

***Corresponding author:**
Yang Qi
(qiyang6@163.com)

Citation: Huang G, Yang H, Nie X, Qi Y. Anisotropy of room- and high-temperature mechanical properties in GH5188 superalloy fabricated by laser powder bed fusion. *Mater Sci Add Manuf*. 2026;5(3):026040009. doi: 10.36922/MSAM026040009

Received: January 24, 2026

Revised: February 25, 2026

Accepted: March 5, 2026

Published online: May 18, 2026

Copyright: © 2026 Author(s). This is an Open-Access article distributed under the terms of the Creative Commons Attribution License, permitting distribution, and reproduction in any medium, provided the original work is properly cited.

Publisher's Note: AccScience Publishing remains neutral with regard to jurisdictional claims in published maps and institutional affiliations.

1. Introduction

GH5188 is a Co–Ni–Cr–W solid-solution strengthened superalloy renowned for its exceptional high-temperature strength and oxidation resistance up to approximately 900 °C.[1] This alloy is widely used for components such as combustor cans, transition ducts, and other high-temperature gas-path structures where the material must sustain mechanical loading under severe thermo-oxidative conditions.[2] Conventionally, these components are manufactured by casting and/or wrought processing, followed by heat treatment to stabilize the microstructure and achieve the required balance of strength and ductility.[3] However, the growing demand for complex, integrated designs and shorter production cycles in the aerospace industry is pushing the limits of conventional manufacturing.[4,5]

Additive manufacturing, particularly laser powder bed fusion (LPBF), offers an attractive route to fabricate geometrically complex metallic components with reduced lead time and material waste,[6-8] while enabling more flexible design and manufacturing workflows.[9,10] LPBF is increasingly combined with data-driven alloy and process optimization to accelerate materials development and enable microstructure-based property tailoring.[11,12] LPBF could enable near-net-shape production of GH5188 turbine parts that were previously infeasible to make by casting or forging.[13] Research on LPBF-fabricated GH5188 began relatively late and remained limited until recently.[13-19] Previous investigations on LPBF-fabricated GH5188 have primarily concentrated on microstructural characteristics and room-temperature mechanical performance. These studies consistently showed that LPBF processing produced a hierarchical structure with strong crystallographic texture along the build direction, which is inherently associated with directional mechanical behavior.[20-23] For instance, LPBF GH5188 typically developed elongated grains with a preferred <001> orientation and sub-micron cellular features enriched in segregated alloying elements, resulting in strength levels that can exceed those of wrought or cast counterparts.[13] Orientation-dependent tensile responses have also been experimentally verified, showing that vertical specimens exhibited lower YS than horizontal ones because the load axis aligns with elongated columnar grains.[16] Such findings establish that anisotropy is a fundamental characteristic of LPBF GH5188 and must be considered when designing structural components.

By contrast, studies addressing elevated-temperature behavior or post-processing effects were comparatively limited and often lacked orientation resolution. Heat-treatment investigations demonstrated that solution or aging treatments could substantially modify microstructure and mechanical properties by altering carbides, dislocation density, and recrystallization state, with solution-treated material showing improved ductility and good tensile performance even at 900 °C.[19] Other works focused on process-induced defects and failure mechanisms rather than directional mechanical response; for example, cracking in LPBF GH5188 has been linked to grain-boundary characteristics and solidification conditions.[17] Process-modification approaches such as ultrasonic-assisted LPBF have been explored to refine grains, weaken texture, and thereby reduce anisotropy, but these studies mainly evaluated overall property improvements rather than systematically quantifying orientation-dependent behavior.[14] Collectively, these works demonstrated that temperature, microstructure, and post-processing each influenced performance, yet they were typically examined independently.

Therefore, a lack of systematic datasets remained that simultaneously resolve mechanical anisotropy across orientations and temperatures for LPBF GH5188, together with an insufficient understanding of how heat treatment modifies such anisotropy. Addressing this gap is essential because deformation mechanisms at service-relevant temperatures can differ fundamentally from those at room temperature, meaning orientation effects observed at ambient conditions cannot be directly extrapolated.

The present study focused on evaluating the anisotropic mechanical properties of LPBF-fabricated GH5188 across different orientations and assessing the influence of solution treatment on those properties. Specifically, tensile tests were conducted both at room temperature and at a high service-relevant temperature of 900 °C on samples built in vertical and horizontal orientations, in both the as-fabricated state and after solution heat treatment. Microstructural examinations were used to correlate the mechanical behavior with features such as substructure, grain morphology, and precipitates. This work provides orientation-aware mechanical data and mechanistic interpretation that support the qualification and design of LPBF GH5188 hot-section components.

2. Materials and methods

A gas-atomized GH5188 alloy powder (Avimetal AM Tech Co., Ltd., China) with the chemical composition presented in Table 1 was employed as the feedstock for LPBF using an EOS M290 system (EOS GmbH, Germany). Dense specimens with a relative density exceeding 99.9% were fabricated under a laser power of 250 W, a scanning speed of 1,000 mm/s, a hatch spacing of 0.08 mm, and a layer thickness of 40 μm, with a strip scanning strategy (10 mm stripe width) and a 67° interlayer hatch rotation. The build plate was preheated to 100 °C, and processing was conducted under an argon atmosphere with the oxygen content maintained below 100 ppm. The relative density was evaluated by optical image analysis (Media Cybernetics, USA). All specimens were prepared using standard metallographic procedures. Cross-sectional optical micrographs were acquired using an EPIPHOT 300 optical microscope (Nikon, Japan). For each condition, 10 micrographs were analyzed using ImagePro software

(Media Cybernetics, USA) to quantify the porosity area fraction and determine the relative density. Two categories of samples were investigated: as-fabricated (AF) and heat-treated (HT). The HT specimens were heated from room temperature to 1,180 °C at a rate of 10 °C/min in a KSL-1400X muffle furnace (Kejing Auto-instrument Co., Ltd. China) , held at 1,180 °C for 1 h, and subsequently cooled to room temperature in air.

Figure 1 schematically summarizes the specimen geometry and the orientation definitions adopted in this work, including the tensile loading directions and the planes selected for microstructural analysis (scanning electron microscope [SEM]/electron backscatter diffraction [EBSD]) with respect to the build direction. Dog-bone tensile specimens were machined in accordance with ASTM B557M-10, with gauge dimensions of 32 mm in length, 6 mm in width, and 3 mm in thickness. Room-temperature and 900 °C tensile tests were conducted using a Zwick/Roell Z020 universal testing machine with a displacement rate of 1 mm/min. In accordance with ISO 6892-2:2018, each specimen was equilibrated at the test temperature for 10 minutes prior to loading. Three replicate tests were performed for each sample condition to ensure reproducibility. Scanning electron microscopy was performed using a Zeiss Gemini 300 field emission SEM (Carl Zeiss Microscopy GmbH, Germany). EBSD data were acquired on the same instrument equipped with an EBSD detector (Symmetry S3 EBSD detector, Oxford Instruments NanoAnalysis, UK), and the resulting datasets were post-processed using AZtecCrystal software (Version 2.1, Oxford Instruments NanoAnalysis, UK).

3. Results

3.1. Mechanical properties

Figure 2 presents the room–temperature tensile stress–strain curves of LPBF-fabricated GH5188 alloy along the horizontal and vertical directions for both AF and HT conditions, with the corresponding tensile properties summarized in Table 2. The AF specimens showed high strength and moderate ductility, with yield strength (YS) values of 812.7 ± 8.1 MPa and 805.3 ± 2.4 MPa in the horizontal and vertical directions, respectively. Their ultimate tensile strength (UTS) exceeded 1,050 MPa for both orientations, accompanied by elongations of 43.6 ± 2.0% (horizontal) and 47.4 ± 2.7% (vertical). Following solution treatment, the YS decreased significantly to 538.1 ± 7.1 MPa and 517.0 ± 4.7 MPa for the horizontal and vertical specimens, respectively, while the UTS remained comparable to that of the AF condition. Despite the substantial reduction in YS, the HT specimens exhibited markedly improved ductility, achieving elongations of approximately 58–60%.

Figure 3 shows the room-temperature tensile fracture morphologies of the LPBF-fabricated GH5188 specimens in both orientations under the AF and HT conditions. All four fracture surfaces exhibited a predominantly ductile morphology characterized by widespread, fine dimples, indicating that failure was governed by microvoid nucleation, growth, and coalescence. This consistent dimpled appearance implies that the room-temperature fracture mode was insensitive to build orientation and heat treatment at the morphological level.

Figure 4 shows the tensile stress–strain curves obtained at 900 °C, with the associated mechanical data also summarized in Table 2. At elevated temperature, all specimens demonstrated significantly reduced strength compared with room-temperature testing, consistent with the expected high-temperature softening behavior of this Co-based superalloy. For the AF condition, the YS decreased to 371.5 ± 2.1 MPa (horizontal) and 361.2 ± 2.4 MPa (vertical), while the UTS was reduced to approximately 366–376 MPa. The HT specimens exhibited an additional decline in high-temperature strength, with

Table 1. Measured powder composition and nominal composition range of GH5188 alloy (wt%)

Element	Co	C	Ni	Cr	W	La	Fe	Si	Cu	P	S	B	Mn	O	N
Powder (measured)	Balance	0.073	23.3	23.3	14.3	0.04	1.2	0.43	0.02	<0.01	0.002	0.003	0.94	0.018	0.006
Nominal GH5188 specification	Balance	0.05–0.15	20–24	20–24	13–16	0.03–0.12	≤3.0	0.2–0.5	≤0.07	≤0.02	≤0.015	≤0.015	≤1.25	≤0.02	≤0.02

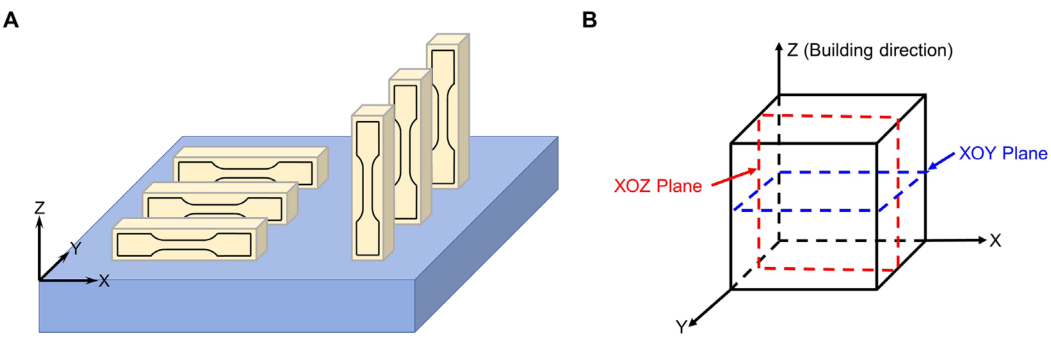

Figure 1. Schematic diagram of sample geometry and sampling orientations. (A) tensile specimens and building directions; (B) sections prepared for microstructural characterization (scanning electron microscope/electron backscatter diffraction) relative to the build direction.

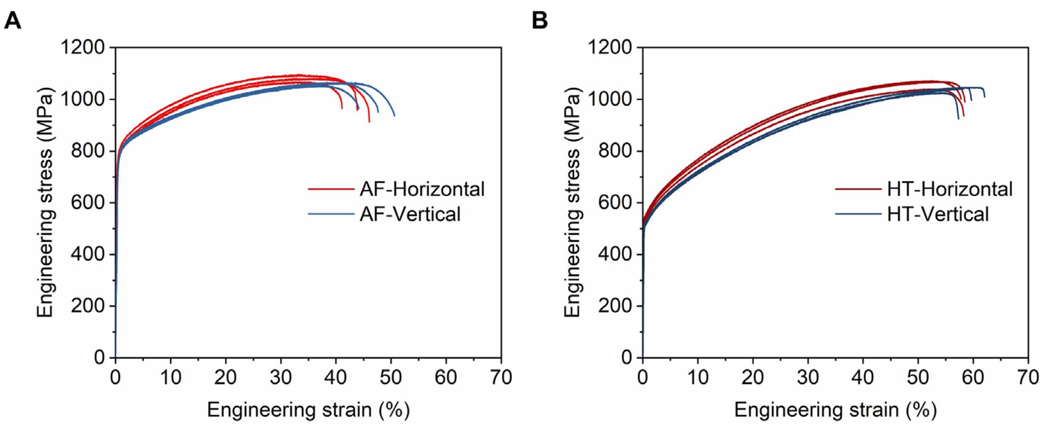

Figure 2. Room-temperature tensile stress–strain curves of LPBF-fabricated GH5188 alloy along the horizontal and vertical directions for (A) AF and (B) HT conditions

Abbreviations: AF: As-fabricated; HT: Heat-treated; LPBF: Laser powder bed fusion.

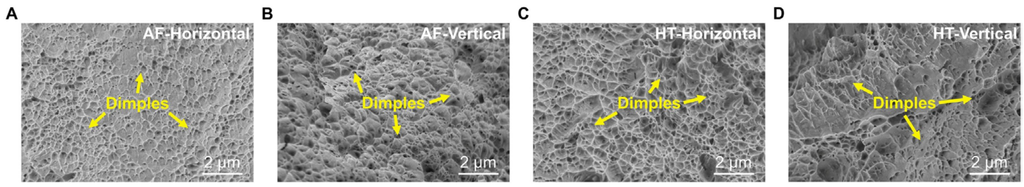

Figure 3. Room-temperature tensile fracture morphologies of LPBF-fabricated GH5188. (A) AF-Horizontal, (B) AF-Vertical, (C) HT-Horizontal, and (D) HT-Vertical. Scale bars: 2 μm; magnification: 10,000×.

Abbreviations: AF: As-fabricated; HT: Heat-treated; LPBF: Laser powder bed fusion.

YS values of 331.8 ± 2.9 MPa (horizontal) and 314.2 ± 5.0 MPa (vertical) and UTS values of 347.1 ± 2.7 MPa (horizontal) and 324.2 ± 3.2 MPa (vertical). Nevertheless, the HT specimens showed significantly enhanced ductility, reaching elongations of 42.2 ± 2.9% (horizontal) and 51.6 ± 4.4% (vertical), surpassing those of the AF samples.

Figure 5 presents the fracture morphologies of the specimens tensile-tested at 900 °C for both build orientations under the AF and HT conditions. In contrast to the dimpled ductile features observed at room temperature (Figure 3), all four samples showed a markedly different surface appearance dominated by relatively smooth, faceted regions, with dimples being largely absent. Such a transition in fracture morphology was consistent with a high-temperature damage process in which thermally activated deformation suppressed extensive microvoid growth within the matrix and promoted fracture through boundary-related separation or facet-like rupture. No obvious differences among these four specimens suggested that the dominant 900 °C fracture mode was broadly similar across orientations and heat-treatment conditions.

These results indicate that heat treatment substantially reduced the YS at room and elevated temperatures while concurrently improving tensile ductility. Moreover, the relatively small differences between horizontal and vertical specimens suggest that LPBF-fabricated GH5188 alloy exhibited minimal tensile anisotropy in the AF condition. By contrast, a more evident anisotropy emerged after heat treatment for the LPBF-fabricated GH5188 alloy, particularly at 900 °C.

3.2. Microstructure

Figure 6 compares the microstructures of LPBF-fabricated GH5188 in the AF and HT states on both the XOZ and XOY sections. In the AF condition, the low-magnification images revealed a characteristic layered melt-pool morphology. Distinct melt-pool boundaries were readily identified as overlapping tracks, reflecting the melt-pool geometry and the layer-by-layer thermal cycling inherent to LPBF. On the XOZ section, the melt-pool boundaries delineated successive layers and highlighted a preferential epitaxial growth tendency along the build direction, indicating that solidification proceeds by partial remelting and competitive growth across layer interfaces rather than by repeated random nucleation. At higher magnification, both AF sections exhibited a well-developed fine cellular solidification substructure, with a continuous cellular network and bright cell walls. Such contrast was consistent with microsegregation during rapid solidification, where solute-enriched regions accumulated at cell boundaries. Discrete nanoscale precipitates were observed in association with this cellular framework (Figure 6, highlighted by arrows), suggesting that the chemically enriched cell walls provide favorable sites for precipitation clustering during solidification and subsequent intrinsic thermal exposure.

After solution treatment, the melt-pool traces and the cellular substructure were no longer discernible in either section, implying substantial homogenization of the solidification-induced chemical gradients and the removal of LPBF-specific mesoscale features. The HT microstructure became comparatively uniform at both length scales, and the remaining second-phase features were limited to sparse nanoscale precipitates. Overall, the AF state exhibited a hierarchical melt-pool/cellular microstructure, which transitioned after solution treatment to a more homogenized matrix containing only

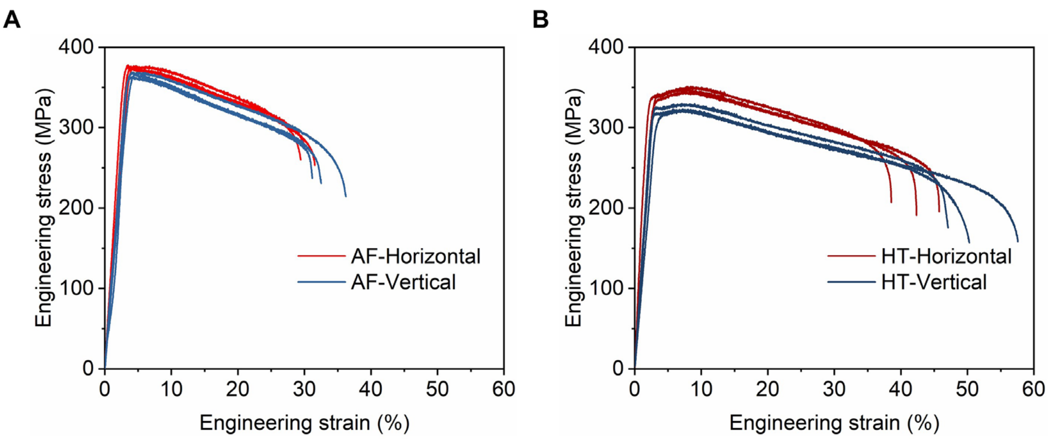

Figure 4. 900 °C tensile stress–strain curves of LPBF-fabricated GH5188 alloy along the horizontal and vertical directions for (A) AF and (B) HT conditions
Abbreviations: AF: As-fabricated; HT: Heat-treated; LPBF: Laser powder bed fusion.

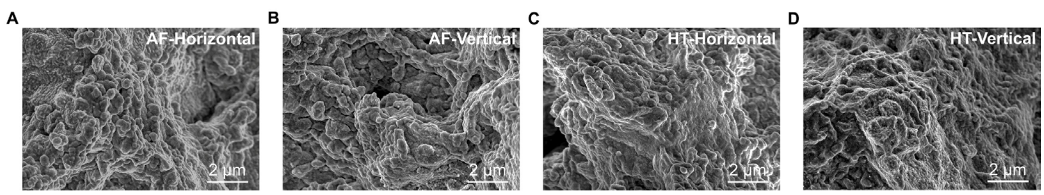

Figure 5. 900 °C tensile fracture morphologies of LPBF-fabricated GH5188. (A) AF-Horizontal, (B) AF-Vertical, (C) HT-Horizontal, and (D) HT-Vertical. Scale bars: 2 μm; magnification: 10,000×.
Abbreviations: AF: As-fabricated; HT: Heat-treated; LPBF: Laser powder bed fusion.

Table 2. Summary of room temperature and 900 °C tensile properties of LPBF-fabricated GH5188 alloy

Sample	Room temperature			900 °C		
	YS (MPa)	UTS (MPa)	Elongation (%)	YS (MPa)	UTS (MPa)	Elongation (%)
AF-Horizontal	812.7 ± 8.1	1078.7 ± 11.3	43.6 ± 2.0	371.5 ± 2.1	375.7 ± 1.2	30.3 ± 0.9
AF-Vertical	805.3 ± 2.4	1058.5 ± 5.7	47.4 ± 2.7	361.2 ± 2.4	366.5 ± 2.7	33.2 ± 2.2
HT-Horizontal	538.1 ± 7.1	1058.1 ± 14.8	58.1 ± 0.3	331.8 ± 2.9	347.1 ± 2.7	42.2 ± 2.9
HT-Vertical	517.0 ± 4.7	1038.0 ± 9.6	59.6 ± 1.9	314.2 ± 5.0	324.2 ± 3.2	51.6 ± 4.4

Abbreviations: AF: As-fabricated; HT: Heat-treated; UTS: Ultimate tensile strength; YS: Yield strength.

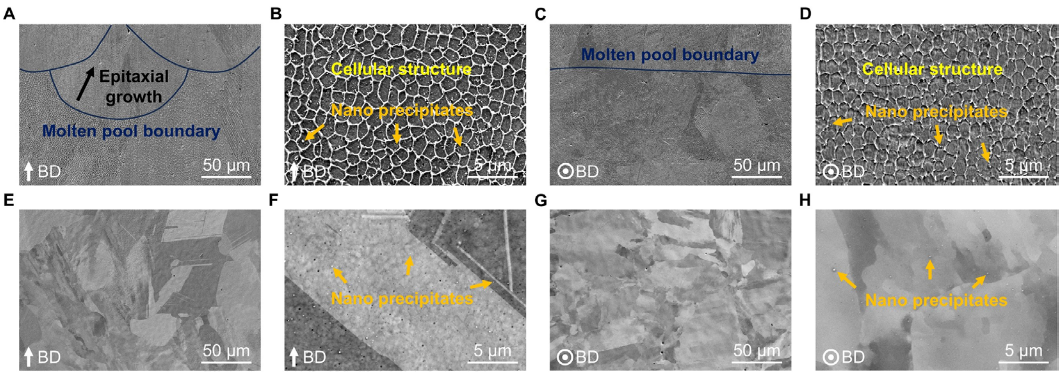

Figure 6. Scanning electron microscopic images of LPBF-fabricated GH5188 alloy: (A–B) AF-XOZ section, (C–D) AF-XOY section, (E–F) HT-XOZ section, and (G–H) HT-XOY section. Scale bars: (A, C, E, G) 50 μm, (B, D, F, H) 5 μm; (A, C, E, G) magnification: 500×, (B, D, F, H) magnification: 5, 000×. Abbreviations: AF: As-fabricated; BD: Building direction; HT: Heat-treated; LPBF: Laser powder bed fusion.

residual nanoscale precipitates in both the XOZ and XOY orientations.

Figure 7 compares the EBSD results of LPBF-fabricated GH5188 in the AF condition on the XOZ and XOY sections, highlighting section-dependent melt-pool signatures, grain morphology, and boundary character. On the XOZ section, the inverse pole figure (IPF) map (Figure 7A) revealed a classical semi-circular melt-pool morphology, with grains curving and elongating along the melt-pool contour, reflecting the layer-by-layer remelting and epitaxial growth across successive tracks. In contrast, the XOY section (Figure 7D) exhibited prominent, nearly straight band-like features that correspond to scan-track/melt-pool boundary traces. Grains were typically elongated and locally arranged with respect to these linear features, indicating that grain morphology was strongly guided by the local thermal gradient and the repetitive raster scanning strategy.

Despite these distinct melt-pool geometries and grain-shape differences, both sections displayed a broad distribution of IPF colors, suggesting weak macroscopic texture in the mapped areas. The XOZ section (Figure 7B) was dominated by high-angle grain boundaries (HAGBs); 80.3%) with a small contribution from low-angle grain boundaries (LAGBs); 19.1%), whereas the XOY section (Figure 7E) contained a higher fraction of HAGBs (87.7%)

and a lower fraction of LAGBs (12.3%). The grain-size distributions indicate that the mean grain size was comparable between the two sections (52.67 μm for XOZ and 49.16 μm for XOY), with both dominated by fine-to-intermediate grains and a limited fraction of coarser grains.

Overall, although the XOZ and XOY sections showed different melt-pool traces and corresponding variations in grain alignment, both sections exhibited similarly weak texture, comparable average grain sizes, and broadly similar boundary networks with HAGBs remaining dominant. Therefore, the microstructural differences between the two sections were not pronounced and were unlikely to cause a significant change in the tensile response, consistent with the minimal anisotropy observed in the AF condition.

Figure 8 shows the EBSD maps of the HT GH5188 and highlights how heat treatment modifies the AF microstructure in a section-dependent manner. The XOZ section exhibited a complete removal of melt-pool traces: the semi-circular melt-pool morphology apparent in the AF condition (Figure 7A) was no longer discernible after heat treatment (Figure 8A), suggesting a stronger homogenization of LPBF-related morphological features on this section. However, grain coarsening was comparatively limited: the average grain size increased only slightly to 61.01 μm from 52.67 μm in the AF XOZ section. In addition, the boundary character in the XOZ section remained dominated by HAGBs (86.6%) with a relatively low LAGB fraction (13.4%) (Figure 8B), broadly comparable to the AF condition.

In the XOY section (Figure 8D), the distinct banded features associated with scan-track/melt-pool boundaries that were clearly visible in the AF condition (Figure 7D) became significantly blurred, indicating that heat treatment largely weakened the melt-pool-scale heterogeneity. Meanwhile, the grains coarsened markedly, as evidenced by the grain-size histogram (Figure 8F), where the average grain size increased from 49.16 μm to 110.41 μm. The grain-boundary statistics also changed substantially (Figure 8E): the HAGB fraction decreased to 58.0% and the LAGB fraction increased to 42.0%, compared with 87.7% HAGBs and 12.3% LAGBs in the AF state (Figure 7E).

Together with the dispersed IPF colors in both sections, these results suggest that heat treatment significantly suppressed the melt-pool/cellular imprint of LPBF and reduced mesoscale heterogeneity, while the extent of grain-growth and boundary-character evolution was anisotropic. The XOY section underwent pronounced grain coarsening accompanied by a strong increase in LAGBs, whereas

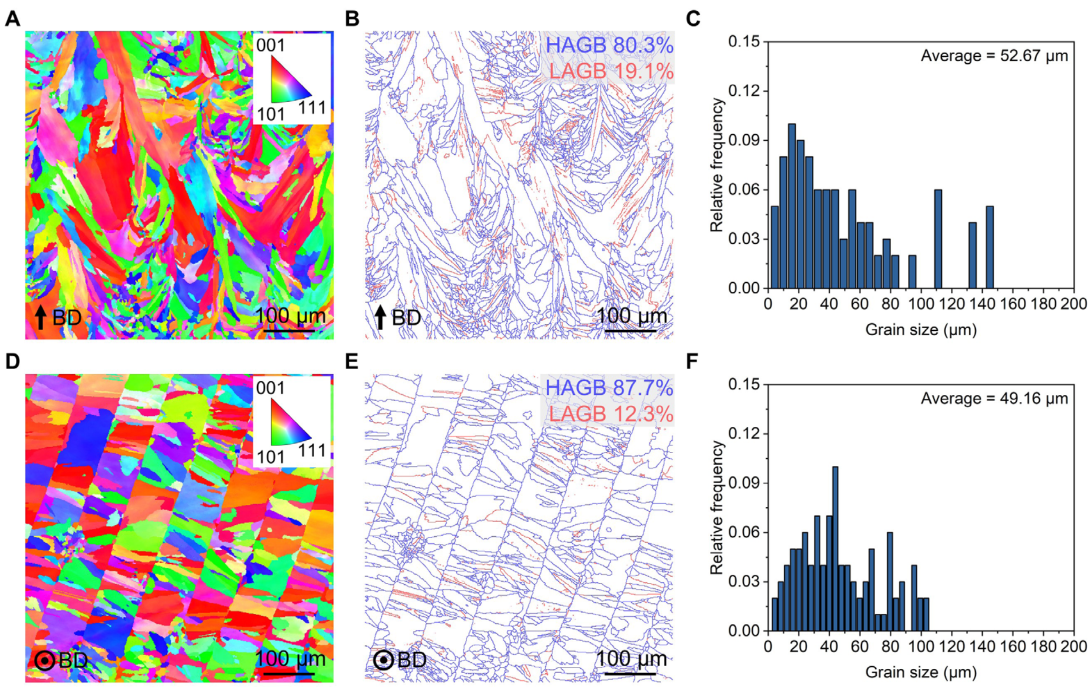

Figure 7. Electron backscatter diffraction characterization of LPBF-fabricated GH5188 alloy in the as-fabricated condition: (A) IPF map, (B) grain boundary map, and (C) grain-size distribution for the XOZ section; (D) IPF map, (E) grain boundary map, and (F) grain-size distribution for the XOY section. Scale bars: (A, B, D, E) 100 μm; magnification: 200×.

Abbreviations: BD: Building direction; HAGB: High-angle grain boundary; IPF: Inverse pole figure; LAGB: Low-angle grain boundary; LPBF: Laser powder bed fusion.

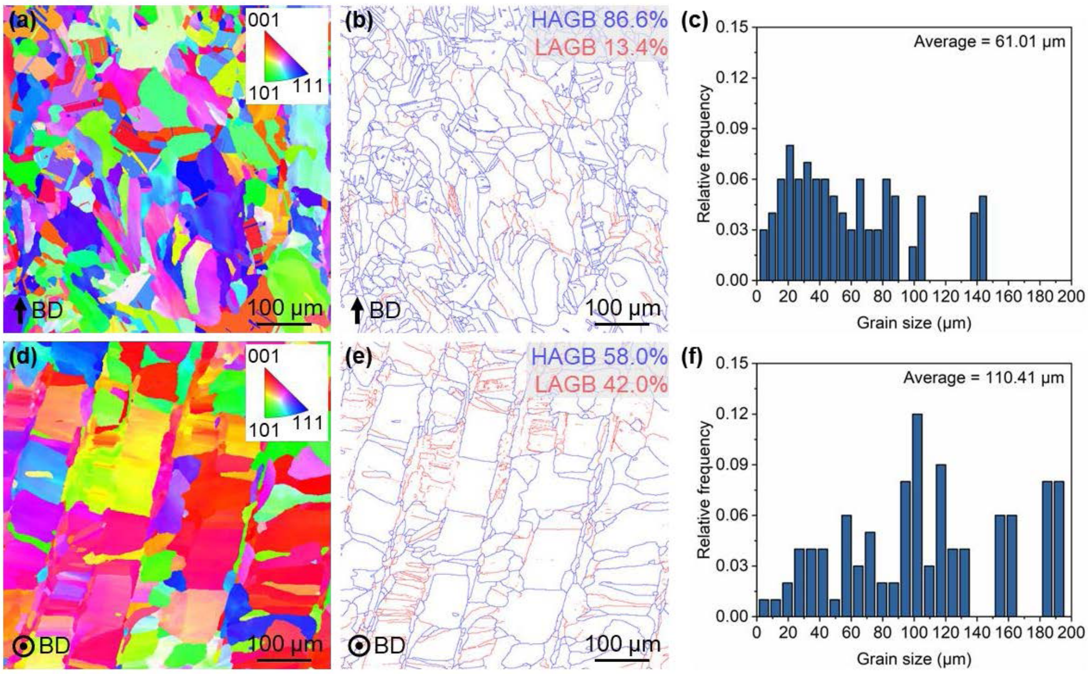

Figure 8. Electron backscatter diffraction characterization of LPBF-fabricated GH5188 alloy in the heat-treated condition: (A) IPF map, (B) grain boundary map, and (C) grain-size distribution for the horizontal XOZ section; (D) IPF map, (E) grain boundary map, and (F) grain-size distribution for the XOY section. Scale bars: (A, B, D, E) 100 μm; magnification: 200×.

Abbreviations: BD: Building direction; HAGB: High-angle grain boundary; IPF: Inverse pole figure; LAGB: Low-angle grain boundary; LPBF: Laser powder bed fusion.

the XOZ section showed a more moderate grain-size change and retained a high fraction of HAGBs. This section-dependent microstructural evolution provided an important basis for interpreting the changes in mechanical anisotropy between the AF and HT conditions.

4. Discussion

4.1. Room temperature strengthening mechanism

At room temperature, the YS of LPBF-fabricated GH5188 is governed by both conventional contributions (solid-solution strengthening,[24] grain boundaries,[25] and second phases[26]) and LPBF-specific features, especially the fine cellular network and the associated high dislocation density generated by rapid solidification and repeated thermal cycling. In the AF condition, cellular boundaries and solute-enriched walls (Figure 6) provide a high density of obstacles to dislocation motion, which explains the high YS relative to the heat-treated state.

The weak tensile anisotropy at room temperature is consistent with the broadly similar microstructure between orientations: EBSD indicates weak macroscopic texture and comparable grain sizes (Figure 7), and the cellular/substructure scale is similar across sections (Figure 6). After heat treatment, the melt-pool/cellular imprint is largely removed and recovery/homogenization reduces the initial obstacle density (Figure 6), which lowers YS but enables more uniform plastic deformation and improved elongation. Because the post-heat-treatment microstructure remains weakly textured and both orientations share the same alloy chemistry and heat-treatment history, only minor orientation effects are expected at room temperature.

4.2. High temperature strengthening mechanism

At 900 °C, the strength of GH5188 decreased substantially relative to room temperature (Table 2), reflecting the temperature dependence of the elastic constants, enhanced dislocation climb, and dynamic recovery.[27] Under these conditions, strength is governed less by athermal barriers and more by thermally activated mechanisms.[28] The principal contributors can be summarized as: (i) solid-solution strengthening from refractory elements (e.g., W and Cr), which can retard dislocation climb and diffusion-mediated processes;[29] (ii) the stability and distribution of carbides/second phases that pin dislocations and grain boundaries;[28] and (iii) grain-boundary mediated deformation, which becomes increasingly relevant as temperature approaches a significant fraction of the melting temperature.[30]

A key observation is that the AF specimens exhibited higher high-temperature YS/UTS than the HT specimens in both orientations, whereas the HT condition showed substantially improved elongation (Table 2). This trend suggests that the LPBF-inherited cellular/substructure hierarchy present in the AF condition remained mechanically relevant during short-term tensile loading at 900 °C. Even if partial recovery occurred rapidly at high temperature, the AF state started from a microstructure containing dense dislocation networks and chemically heterogeneous cellular walls, which could provide additional resistance to plastic flow at the onset of deformation. In contrast, heat treatment removed melt-pool/cellular features (Figure 6), thereby lowering the initial obstacle density to plasticity at 900 °C and promoting larger uniform deformation.

4.3. Enhanced 900 °C mechanical anisotropy after heat treatment

Compared with the AF state, heat treatment led to a clearer orientation dependence of strength at 900 °C (Table 2). This is noteworthy because many LPBF GH5188 studies report anisotropy mainly in the as-built condition and primarily at room temperature, often attributed to columnar grains and texture relative to the loading axis.[13,15]

A plausible explanation is that heat treatment changed which microstructural length scale dominates deformation. In the AF condition, strength was strongly influenced by the fine cellular network, solute-enriched cell walls, and high defect density inherited from rapid solidification (Figure 6), and these LPBF-specific features were similar in both orientations, which can mask grain-scale differences. After heat treatment, the cellular/melt-pool feature was largely removed and the microstructure became more homogeneous (Figure 6), reducing the density of intragranular obstacles. Consequently, the mechanical response became more sensitive to grain size, grain morphology, and the grain-boundary network. Because our HT specimens exhibited section-dependent grain size and boundary character (Figure 8), these differences could translate into an enhanced anisotropy, especially at 900 °C, where grain-boundary mediated deformation contributes more substantially.

Nevertheless, the attribution of the enhanced anisotropy at 900 °C to post-heat treatment grain and boundary character should be viewed as plausible rather than exclusive. At this temperature, thermally activated mechanisms such as dislocation climb and dynamic recovery can rapidly attenuate the influence of the initial microstructure.[31,32] The microstructure may evolve during deformation via recovery, boundary rearrangement, and dynamic recrystallization.[33]

4.4. Work hardening behavior

At room temperature, the work-hardening response reflected the competition between dislocation storage and recovery. The AF specimens began with a high dislocation density and strong cellular strengthening, which raised YS. However, the additional hardening capacity was reduced because the dislocation density increased less during straining and local recovery could be activated more readily.[34] After heat treatment, the initial dislocation density was reduced and the microstructure became more homogeneous. This delayed strain localization and increased strain-hardening capacity, producing substantially higher elongation while maintaining comparable UTS despite the pronounced decrease in YS.

At 900 °C, work hardening was intrinsically limited because climb-assisted recovery rapidly annihilates stored dislocations.[35] Accordingly, the AF condition showed post-yield softening, consistent with the rapid degradation of the LPBF-inherited cellular hierarchy at high temperature. The HT condition could exhibit a small initial positive hardening because it started from a lower obstacle density. Early-stage dislocation multiplication and substructure formation might briefly outpace recovery before a steady-state balance is reached.[36]

5. Conclusion

This study evaluated the tensile anisotropy of LPBF-fabricated GH5188 at room temperature and at the service-relevant temperature (900 °C) by testing specimens oriented parallel and perpendicular to the build direction, and by determining how heat treatment modified this behavior. Microstructural characterization was performed to link the measured responses to underlying features, including substructure, grain morphology, and precipitate evolution. The main conclusions are as follows:

(i) At room temperature, LPBF GH5188 exhibited only a small tensile anisotropy in both AF and HT states: the AF condition showed high YS with moderate ductility, whereas heat treatment reduced YS while maintaining comparable ultimate tensile strength and markedly improving elongation. At 900 °C, all conditions softened substantially, with the AF condition retaining higher YS/UTS than HT in both orientations; meanwhile, ductility increased after heat treatment and the orientation dependence became more evident, with the vertical HT specimens exhibiting higher elongation than the horizontal HT specimens.

(ii) The AF state was characterized by hierarchical LPBF features, including layered melt-pool morphology and a fine cellular substructure with solute-enriched cell walls and nanoscale precipitates, while EBSD indicated weak texture and broadly comparable grain sizes (~49–53 μm) between sections, with HAGBs remaining dominant. After heat treatment, melt-pool traces and the cellular network were no longer discernible, consistent with substantial homogenization; however, EBSD revealed section-dependent grain/boundary evolution, with limited grain coarsening and HAGB-dominated boundaries in XOZ, but pronounced grain coarsening and a strong increase in LAGB fraction in XOY.

(iii) The weak anisotropy in the AF condition was consistent with the dominant contribution of LPBF-inherited cellular strengthening and the relatively weak texture differences. After heat treatment, the removal of LPBF-specific substructure lowered the initial obstacle density and increased ductility, while the mechanical response became more sensitive to differences in grain structure and boundary networks. This contributed to the more evident anisotropy observed in the HT state at 900 °C. This interpretation should be viewed as plausible rather than exclusive, because thermally activated mechanisms can attenuate the influence of the initial microstructure at 900 °C.

Overall, the key contribution of this work is the orientation-resolved comparison of AF and HT LPBF GH5188 alloy at both room temperature and 900 °C, which clarifies how post-processing modifies anisotropy under high-temperature loading and provides data support for the qualification and design of LPBF GH5188 hot-section components.

Acknowledgments

None

Funding

This work was supported by the Taihang Laboratory Project (No. BK123) and the National Natural Science Foundation of China (Nos. 52305490 and 62505373).

Conflict of interest

The authors declare that they have no known competing financial interests or personal relationships that could have appeared to influence the work reported in this paper.

Author contributions

Conceptualization: Yang Qi
Data curation: Yang Qi
Investigation: Gao Huang, Huihui Yang
Methodology: Gao Huang, Xiaojie Nie
Supervision: Yang Qi
Writing–original draft: Gao Huang
Writing–review & editing: Huihui Yang, Xiaojie Nie, Yang Qi

Ethics approval and consent to participate

Not applicable.

Consent for publication

Not applicable.

Availability of data

Data will be made available upon reasonable request to the corresponding author.

References

1. Liu D, Chai H, Yang L, Qiu W, Guo Z, Wang Z. Study on the dynamic recrystallization mechanisms of GH5188 superalloy during hot compression deformation. *J Alloys Compd*. 2022;895:162565.

   doi: 10.1016/j.jallcom.2021.162565

2. Wang X, Luo G, Sun Y, *et al*. Effect of strain rate and high temperature on quasi-static and dynamic compressive behavior of forged GH5188 superalloy. *Mater Sci Eng A*. 2023;886:145391.

   doi: 10.1016/j.msea.2023.145391

3. Lee WS, Kao HC. High temperature deformation behaviour of Haynes 188 alloy subjected to high strain rate loading. *Mater Sci Eng A*. 2014;594:292-301.

   doi: 10.1016/j.msea.2013.11.076

4. Gu D, Shi X, Poprawe R, Bourell DL, Setchi R, Zhu J. Material-structure-performance integrated laser-metal additive manufacturing. *Science*. 2021;372(6545):eabg1487.

   doi: 10.1126/science.abg1487

5. Zhao Z, Jia C, Li Y, *et al*. Microstructure and mechanical properties of additively manufactured GH4099 superalloy. *Mater Sci Addit Manuf*. 2025;4(4):25220047.

   doi: 10.36922/msam025220047

6. Locatelli G, Bocchi S, Quarto M, D'Urso G. Laser powder bed fusion of atomized industrial waste-derived Inconel 725 alloy powders: A machine learning-assisted process optimization. *Mater Sci Addit Manuf*. 2025;5(1):025320072.

   doi: 10.36922/msam025320072

7. Enrique PD, Minasyan T, Toyserkani E. Laser powder bed fusion of difficult-to-print γ' Ni-based superalloys: A review of processing approaches, properties, and remaining

challenges. *Addit Manuf*. 2025;106:104811.

doi: 10.1016/j.addma.2025.104811

8. Mostafaei A, Ghiaasiaan R, Ho IT, *et al*. Additive manufacturing of nickel-based superalloys: A state-of-the-art review on process-structure-defect-property relationship. *Prog Mater Sci*. 2023;136:101108.

doi: 10.1016/j.pmatsci.2023.101108

9. Su J, Ng WL, An J, Yeong WY, Chua CK, Sing SL. Achieving sustainability by additive manufacturing: a state-of-the-art review and perspectives. *Virtual Phys Prototyp*. 2024;19(1):e2438899.

doi: 10.1080/17452759.2024.2438899

10. Su JL, Jiang FL, Teng J, *et al*. Laser additive manufacturing of titanium alloys: process, materials and post-processing. *Rare Met*. 2024;43(12):6288-6328.

doi: 10.1007/s12598-024-02685-x

11. Su J, Li Q, Teng J, *et al*. Programmable mechanical properties of additively manufactured novel steel. *Int J Extrem Manuf*. 2024;7(1):015001.

doi: 10.1088/2631-7990/ad88bc

12. Su J, Chen L, Van Petegem S, *et al*. Additive manufacturing metallurgy guided machine learning design of versatile alloys. *Mater Today*. 2025;88:240-250.

doi: 10.1016/j.mattod.2025.06.031

13. Wei W, Xiao JC, Wang CF, *et al*. Hierarchical microstructure and enhanced mechanical properties of SLM-fabricated GH5188 Co-superalloy. *Mater Sci Eng A*. 2022;831:142276.

doi: 10.1016/j.msea.2021.142276

14. Yan Z, Trofimov V, Song C, *et al*. Microstructure and mechanical properties of GH5188 superalloy additively manufactured via ultrasonic-assisted laser powder bed fusion. *J Alloys Compd*. 2023;939:168771.

doi: 10.1016/j.jallcom.2023.168771

15. Liu Y, Huang Z, Zhang C, *et al*. Microstructure and mechanical properties of Haynes 188 alloy manufactured by laser powder bed fusion. *Mater Charact*. 2024;211:113880.

doi: 10.1016/j.matchar.2024.113880

16. Liu Y, Huang Z, Zhang C, *et al*. Tailoring microstructure and twin-induced work hardening of a laser powder bed fusion manufactured Haynes 188 alloy. *Mater Sci Eng A*. 2024;891:145925.

doi: 10.1016/j.msea.2023.145925

17. Wu Y, Sun B, Chen B, *et al*. Cracking mechanism of GH5188 alloy during laser powder bed fusion additive manufacturing. *Mater Charact*. 2024;207:113548.

doi: 10.1016/j.matchar.2023.113548

18. Miao L, Wei H, Yue J, *et al*. Superior mechanical properties of a high temperature Co-based superalloy fabricated by laser powder bed fusion. *Addit Manuf Lett*. 2025;14:100311.

doi: 10.1016/j.addlet.2025.100311

19. Yang B, Liu Y, Qi Y, *et al*. Effects of heat treatment on microstructure and mechanical properties of GH5188 superalloy fabricated by Selective laser melting. *Mater Sci Eng A*. 2025;946:149084.

doi: 10.1016/j.msea.2025.149084

20. Mukherjee T, Elmer JW, Wei HL, *et al*. Control of grain structure, phases, and defects in additive manufacturing of high-performance metallic components. *Prog Mater Sci*. 2023;138:101153.

doi: 10.1016/j.pmatsci.2023.101153

21. Chandra S, Radhakrishnan J, Huang S, Wei S, Ramamurty U. Solidification in metal additive manufacturing: challenges, solutions, and opportunities. *Prog Mater Sci*. 2025;148:101361.

doi: 10.1016/j.pmatsci.2024.101361

22. Zhu Z, Hu Z, Seet HL, *et al*. Recent progress on the additive manufacturing of aluminum alloys and aluminum matrix composites: Microstructure, properties, and applications. *Int J Mach Tools Manuf*. 2023;190:104047.

doi: 10.1016/j.ijmachtools.2023.104047

23. Niu Z, Zhang J, Liu F, *et al*. Forming quality control of Laser Powder Bed Fusion GH3536 alloy: Surface quality, defects, and microstructure. *Mater Sci Addit Manuf*. 2025;4(4):025220042.

doi: 10.36922/msam025220042

24. Yang B, Shang Z, Ding J, *et al*. Investigation of strengthening mechanisms in an additively manufactured Haynes 230 alloy. *Acta Mater*. 2022;222:117404.

doi: 10.1016/j.actamat.2021.117404

25. Hansen N. Hall–Petch relation and boundary strengthening. *Scr Mater*. 2004;51(8):801-806.

doi: 10.1016/j.scriptamat.2004.06.002

26. Yang X, Qi Y, Zhang W, Wang Y, Zhu H. Laser powder bed fusion of C18150 copper alloy with excellent comprehensive properties. *Mater Sci Eng A*. 2023;862:144512.

doi: 10.1016/j.msea.2022.144512

27. Yang C, Chen X, Tian Y, *et al*. High-temperature oxidation behavior of SLM-processed and forged GH5188 Co-based superalloy. *Smart Mater Manuf*. 2025;3:100093.

doi: 10.1016/j.smmf.2025.100093

28. Haack M, Kuczyk M, Seidel A, López E, Brueckner F, Leyens C. Comprehensive study on the formation of grain boundary serrations in additively manufactured Haynes 230 alloy. *Mater Charact*. 2020;160:110092.

doi: 10.1016/j.matchar.2019.110092

29. Galindo-Nava EI, Schlütter R, Messé OMDM, Argyrakis C, Rae CMF. A model for dislocation creep in polycrystalline Ni-base superalloys at intermediate temperatures. *Int J Plast*. 2023;169:103729.

    doi: 10.1016/j.ijplas.2023.103729

30. Yoon JG, Jeong HW, Yoo YS, Hong HU. Influence of initial microstructure on creep deformation behaviors and fracture characteristics of Haynes 230 superalloy at 900 °C. *Mater Charact*. 2015;101:49-57.

    doi: 10.1016/j.matchar.2015.01.002

31. Tang YT, D'Souza N, Roebuck B, Karamched P, Panwisawas C, Collins DM. Ultra-high temperature deformation in a single crystal superalloy: Mesoscale process simulation and micromechanisms. *Acta Mater*. 2021;203:116468.

    doi: 10.1016/j.actamat.2020.11.010

32. Feng J, Wang B, Zhang Y, *et al*. High-temperature creep mechanism of Ti-Ta-Nb-Mo-Zr refractory high-entropy alloys prepared by laser powder bed fusion technology. *Int J Plast*. 2024;181:104080.

    doi: 10.1016/j.ijplas.2024.104080

33. Li Y, Jiang Z, Li L, Xie G, Zhang J, Feng Q. Dynamic recovery and recrystallization of an as-cast SX superalloy during hot deformation. *J Mater Sci Technol*. 2025;217:296-310.

    doi: 10.1016/j.jmst.2024.08.031

34. Markovic P, Scheel P, Wróbel R, Leinenbach C, Mazza E, Hosseini E. Cyclic mechanical response of LPBF Hastelloy X over a wide temperature and strain range: Experiments and modelling. *Int J Solids Struct*. 2024;305:113047.

    doi: 10.1016/j.ijsolstr.2024.113047

35. Zhou J, Su B, Zhu G, *et al*. High-temperature tensile properties of laser powder bed fusion Ti–6.5Al–2Zr–1Mo–1V alloy after annealing. *Mater Sci Eng A*. 2025;923:147700.

    doi: 10.1016/j.msea.2024.147700

36. Pham MS, Iadicola M, Creuziger A, Hu L, Rollett AD. Thermally-activated constitutive model including dislocation interactions, aging and recovery for strain path dependence of solid solution strengthened alloys: Application to AA5754-O. *Int J Plast*. 2015;75:226-243.

    doi: 10.1016/j.ijplas.2014.09.010